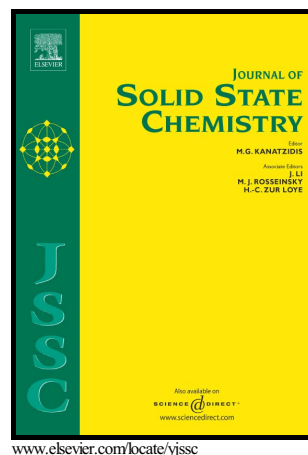


Author's Accepted Manuscript

MoO₃@SiO₂ nanoreactors: synthesis with a thermal decomposition strategy and catalysis on alkenes epoxidation

Yirui Shen, Pingping Jiang, Yingchun Wang, Gang Bian, Phyu Thin Wai, Yuming Dong



PII: S0022-4596(18)30183-X
DOI: <https://doi.org/10.1016/j.jssc.2018.05.005>
Reference: YJSSC20211

To appear in: *Journal of Solid State Chemistry*

Received date: 18 February 2018
Revised date: 17 April 2018
Accepted date: 5 May 2018

Cite this article as: Yirui Shen, Pingping Jiang, Yingchun Wang, Gang Bian, Phyu Thin Wai and Yuming Dong, MoO₃@SiO₂ nanoreactors: synthesis with a thermal decomposition strategy and catalysis on alkenes epoxidation, *Journal of Solid State Chemistry*, <https://doi.org/10.1016/j.jssc.2018.05.005>

This is a PDF file of an unedited manuscript that has been accepted for publication. As a service to our customers we are providing this early version of the manuscript. The manuscript will undergo copyediting, typesetting, and review of the resulting galley proof before it is published in its final citable form. Please note that during the production process errors may be discovered which could affect the content, and all legal disclaimers that apply to the journal pertain.

MoO₃@SiO₂ nanoreactors: synthesis with a thermal decomposition strategy and catalysis on alkenes epoxidation

Yirui Shen, Pingping Jiang, Yingchun Wang, Gang Bian, Phyu Thin Wai, Yuming Dong*

Key Laboratory of Synthetic and Biological Colloids (Jiangnan University), Ministry of Education, School of Chemical and Material Engineering, Wuxi 214122, PR China.

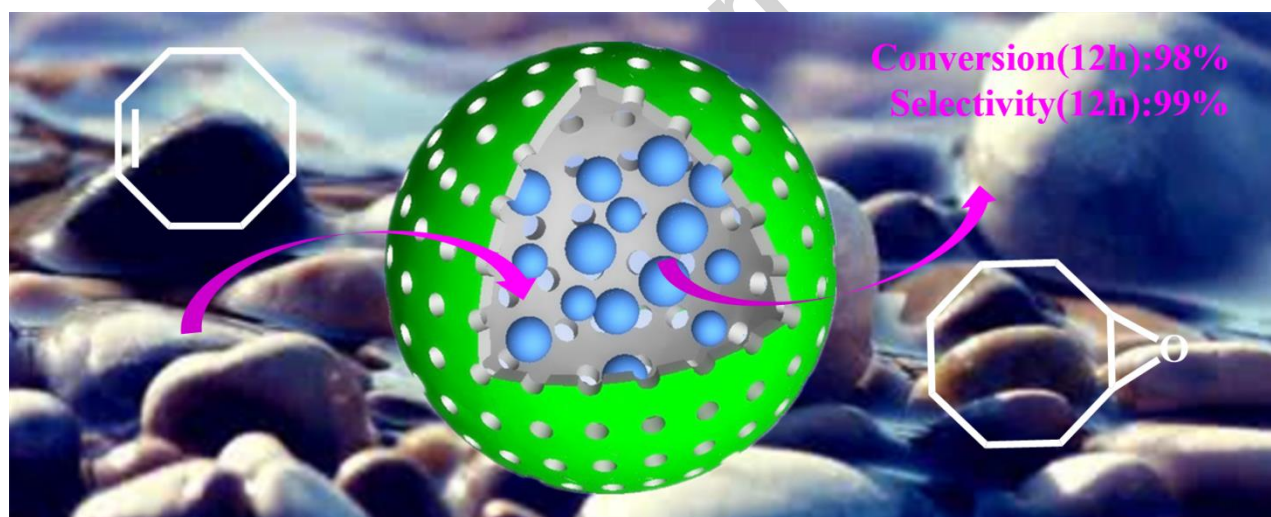
*Corresponding author E-mail addresses: ppjiang@jiangnan.edu.cn.

ABSTRACT:

A general thermal decomposition strategy is reported to fabricate MoO₃@SiO₂ nanoreactors, with a mesoporous silica shell and embedded MoO₃ nanoparticles. The novel preparation procedure involves mixing certain mass ratio of (NH₄)₆Mo₇O₂₄·4H₂O (AMM) and hollow mesoporous silica spheres (HMSS) by grinding, fusion and thermal decomposition of (NH₄)₆Mo₇O₂₄·4H₂O under calcination and removing the residual via filtration. The as-prepared MoO₃@SiO₂ nanoreactors were characterized by X-ray diffraction (XRD), scanning electron microscopy (SEM), transmission electron microscopy (TEM), thermogravimetric analysis (TGA), N₂ adsorption/desorption and X-ray photoelectron spectra (XPS). The nanoreactors were

utilized in epoxidation of alkenes and displayed high catalytic activity and stability. The mass ratio of AMM and HMSS greatly affected the properties and catalytic performance of the nanoreactors. The optimal mass ratio of AMM: HMSS has been confirmed as 1/2. After reacting for 12 h with H_2O_2 (50 wt%) as oxidant, conversion and selectivity of optimal $\text{MoO}_3@\text{SiO}_2$ -400-1/2 almost reached up to 98% and 99%, respectively. Furthermore, the catalyst still had high conversion (78 %) and selectivity (95 %) at 4 h epoxidation of cyclooctene after recycling for 6 runs. Kinetics study was also carried out and demonstrated the epoxidation of alkenes follows the first order model.

Graphical abstract



A thermal decomposition strategy is employed to fabricate $\text{MoO}_3@\text{SiO}_2$ nanoreactors with a mesoporous silica shell and embedded MoO_3 nanoparticles, showing promising reactivity and stability in epoxidation of alkenes.

Keywords: Thermal decomposition; Molybdenum trioxide; Nanoreactor; Alkenes; Epoxidation

1. Introduction

For a variety of applications in the fields of catalysis [1], delivery [2], lithium-ion batteries [3] and biosensors [4] et al., yolk-shell nanomaterials with movable cores and porous shells are promising platforms, endowed by their tailorability and functionality in both the interior cores and exterior hollow shells. Yolk-shell nanomaterials with core@void@shell nanostructure are potential candidates as nanoreactors for various applications, owing to their easy functionalized cores and hollow shell, the high density of exposed active sites resulting from the movable cores, rapid transportation of reactants and products, the possibility for controlling chemical reactions by using shells with different properties, and the protection effect deriving from the shell during the recycling process [5, 6]. As two major structures of nanoreactors, movable cores and porous shells make prosperous contribution to reactions. In one respect, a permeable shell isolates each movable core in the yolk-shell nanomaterials. Thus, each core will locate in a relatively homogeneous environment, which can greatly promote the contact between reactants [7]. For another, porous shells of the yolk-shell nanoparticles also play a significant role in efficiently preventing the catalytic cores from escaping to the exterior, and simultaneously allowing the easy transportation of reactants and products [8]. To date, yolk-shell materials with noble metal cores have developed rapidly, such as Au@HSNs [9] and Au@TiO₂ [10]. However, the synthesis of yolk-shell materials with transition metals in the core and shell still remains a challenge.

In general, many effective routes have been proposed to incorporate catalytic nanoparticles inside the cavity of the hollow nanoparticles, such as ship-in-bottle means, selective etching or

dissolution approaches, Ostwald ripening strategies, bottom-up methods by soft templating assembly, preparation solutions based on the Kirkendall effect and galvanic replacement routes [11, 12]. K. Soni et al. used incipient wetness impregnation method to modify KIT-6 as effective hydrodesulfurization catalysts. The well-ordered 3-D mesoporous material was successfully developed as support for Mo, CoMo and NiMo and exhibited good activity [13]. Ship-in-bottle strategy is the most renowned method for fabricating yolk-shell nanoparticles. Through this strategy, catalytic cores can grow inside the hollow cavity through self-assembly means or chemical reactions. Ding and co-workers [14] soaked the hollow mesoporous silicas in the molten metal salt hydrate to make the active cores generate in the hollow interior of nanoreactors to construct yolk-shell nanoreactors.

In this work, we developed a $\text{MoO}_3@\text{SiO}_2$ nanoreactor utilized in epoxidation of alkenes according to ship-in-bottle strategy using the melting $(\text{NH}_4)_6\text{Mo}_7\text{O}_{24}\cdot 4\text{H}_2\text{O}$ to introduce active sites MoO_3 into the hollow cavity of hollow mesoporous silica spheres. First, hollow mesoporous silica nanoparticles were fabricated with facial selective etching method. Second, the active sites MoO_3 were introduced by molten AMM and thermal decomposition at certain temperature to produce MoO_3 by absolutely releasing NH_3 and H_2O . Third, the products were filtered to remove the residual MoO_3 . The catalytic activity of $\text{MoO}_3@\text{SiO}_2$ nanoreactor was assessed by epoxidation of cyclooctene with oxidant H_2O_2 (50 wt%) as a probe reaction.

2. Experimental Section

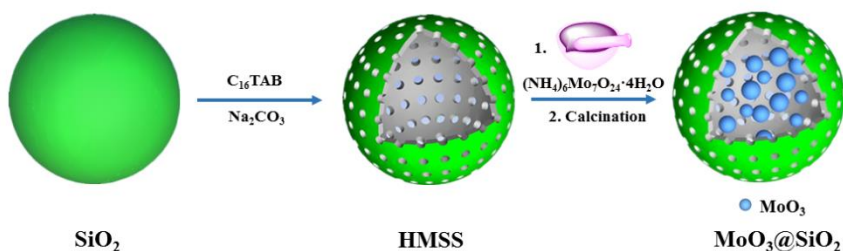
2.1. Materials

Tetraethyl orthosilicate (TEOS), ammonia solution (25-28 wt %), cetyltrimethyl ammonium bromide (C_{16}TAB), anhydrous ethanol, sodium carbonate, hexaammonium heptamolybdate

tetrahydrate $((\text{NH}_4)_6\text{Mo}_7\text{O}_{24}\cdot 4\text{H}_2\text{O}$, AMM) and other solvents were purchased from Sinopharm Chemical Reagent Co. (Shanghai, China). Analytical reagent grade olefins were purchased from Aladdin, China. All the reagents were used without further purification. Deionized water was used all around the experimental process.

2.2. Synthesis of $\text{MoO}_3@\text{SiO}_2$ nanoreactors

The hollow mesoporous silica spheres (HMSS) were obtained after calcination according to our early study [15]. A thermal decomposition strategy was exploited to introduce MoO_3 nanoparticles into shell and cavity referring to Lou's work [14]. A certain amount of $(\text{NH}_4)_6\text{Mo}_7\text{O}_{24}\cdot 4\text{H}_2\text{O}$ (AMM) and hollow mesoporous silica spheres (HMSS) were mixed by grinding. Then the mixture was calcinated at 200 °C for 24 h in the air for complete diffusion of $(\text{NH}_4)_6\text{Mo}_7\text{O}_{24}\cdot 4\text{H}_2\text{O}$ to hollow mesoporous silica spheres through the pores in the shell. After that, the excess $(\text{NH}_4)_6\text{Mo}_7\text{O}_{24}\cdot 4\text{H}_2\text{O}$ and isolated MoO_3 nanoparticles were removed by washing with deionized water and filtrating with membrane. Afterwards the products were dried and denoted as $\text{MoO}_3@\text{SiO}_2\text{-200-X}$, X = AMM: HMSS mass ratio. The products denoted as $\text{MoO}_3@\text{SiO}_2\text{-400-X}$ were obtained by another 6 h calcination at 400 °C after treating at 200 °C for 24 h. The other procedure was the same as $\text{MoO}_3@\text{SiO}_2\text{-200-X}$. The synthetic process was shown in Scheme 1.



Scheme 1. Synthetic process of MoO₃@SiO₂ nanoreactors.

2.3. Alkenes epoxidation

Epoxidation of alkenes was carried out to test the reactivity of catalysts. Alkenes (2.5 mmol), H₂O₂ (50 wt%, 5.0 mmol), n-octane (internal standard, 1.25 mmol) and catalyst (25 mg) were added to acetonitrile (solvent, 10 mL) in a 25 mL two-neck round bottom flask equipped with a reflux condenser at 70 °C. Samples were taken at intervals and stored in the refrigerator. After centrifugation, the supernatant liquid was analyzed by a gas chromatograph (GC, SP-6890A) equipped with a FID detector and a capillary column (SE-54 30m×0.32mm×0.25μm).

2.4. Methods

Scanning electron microscopy (SEM: Hitachi S-4800, 2 kV) and transmission electron microscopy (TEM: JEOL JEM-2100plus, 200 kV) were utilized to detect the morphologies of samples. Nitrogen adsorption/desorption isotherms were determined at -196 °C with nitrogen as analysis gas (Micromeritics ASAP 2010). Surface area measurements were performed according to the Brunauer-Emmett-Teller (BET) method. Thermogravimetric analysis (TGA) of (NH₄)₆Mo₇O₂₄·4H₂O was conducted using TA Instruments (TGA/1100SF). The thermogravimetric analysis (TGA) was ramped at 20 °C·min⁻¹ under a nitrogen flow rate of 50 mL·min⁻¹ from 25 °C to 600 °C. X-ray diffraction (XRD) patterns of the materials were carried out at room temperature using a Rigaku D/MAX-2500PC diffractometer (Rigaku Co., Japan) equipped with Cu-Kα radiation ($\lambda = 1.5418 \text{ \AA}$) and operated at 40 kV and 100 mA. Inductively coupled plasma-mass spectrometry (ICP-MS: NEXION300) was used to analyze the content of molybdenum in materials. X-ray photoelectron spectroscopy (XPS: ESCALAB 250 XI with 200

W Al K α probe beam) and Fourier transform infrared spectroscopy (FT-IR: Nicolet 6700) were used to detect the surface chemical composition of materials.

3. Results and discussion

3.1. Characterization of catalysts

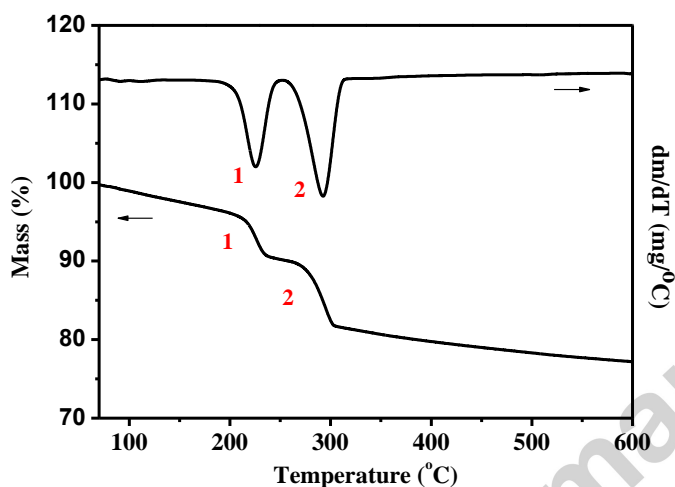


Figure 1. TG curves of $(\text{NH}_4)_6\text{Mo}_7\text{O}_{24}\cdot 4\text{H}_2\text{O}$ in N_2 .



Scheme 2. Decomposition of $(\text{NH}_4)_6\text{Mo}_7\text{O}_{24}\cdot 4\text{H}_2\text{O}$ in air.

Thermal decomposition of $(\text{NH}_4)_6\text{Mo}_7\text{O}_{24}\cdot 4\text{H}_2\text{O}$ was studied under the N_2 flow (Figure 1). Two obvious separated decomposition peaks of the mass loss were observed. The mass loss was accompanied by an endothermic heat effects [16]. The first decomposition step was observed at approximately 225 °C, NH_3 released in parallel with H_2O and $(\text{NH}_4)_2\text{Mo}_4\text{O}_{13}$ appeared [17]. In the second endothermic step (approximately 293 °C), the evolution of NH_3 and H_2O continued

and the phase transformed into MoO_3 . According to the thermal decomposition process, we designed a novel strategy to construct $\text{MoO}_3@\text{SiO}_2$ nanoreactors. AMM and HMSS were mixed by grinding and kept at $200\text{ }^\circ\text{C}$ for 24 h (The melting point of AMM is $190\text{ }^\circ\text{C}$). Under the thermal treatment, the molten AMM would diffuse into the hollow cavity and shell via porous structure in the shell. Meanwhile, NH_3 and H_2O released and $(\text{NH}_4)_6\text{Mo}_7\text{O}_{24}\cdot 4\text{H}_2\text{O}$ transformed into $(\text{NH}_4)_2\text{Mo}_4\text{O}_{13}$. When the temperature continued to increase to $400\text{ }^\circ\text{C}$, the residual NH_3 and H_2O was completely removed to obtain active sites MoO_3 . At the same time, the confined MoO_3 nanoparticles in shell would sinter on the wall. This thermal decomposition strategy was in accordance with the decomposition of $(\text{NH}_4)_6\text{Mo}_7\text{O}_{24}\cdot 4\text{H}_2\text{O}$ under calcination in the air (Scheme 2) [18, 19].

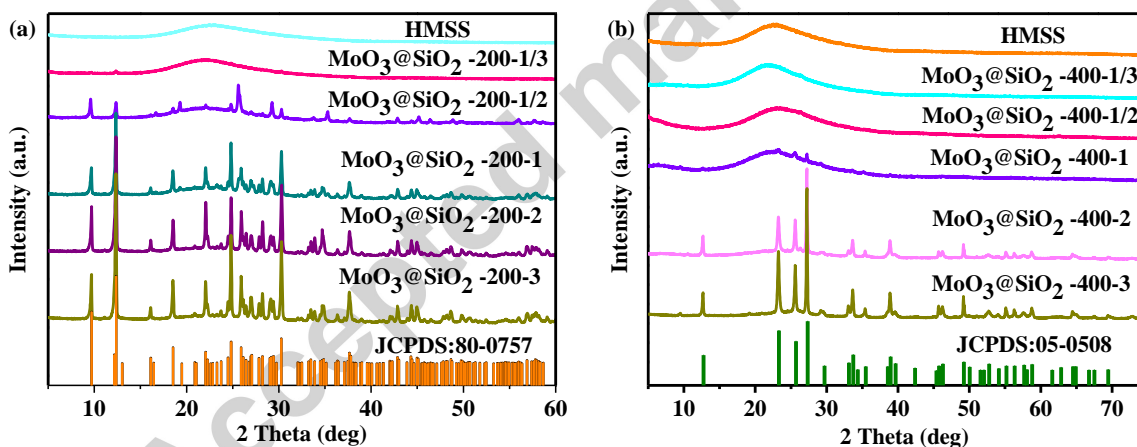


Figure 2. XRD patterns of HMSS, $\text{MoO}_3@\text{SiO}_2$ -200-X (a) and $\text{MoO}_3@\text{SiO}_2$ -400-X (b).

XRD measurement was utilized to certify the crystal structure of samples with different calcination conditions. All the samples indicated a broad peak between 20 ° - 30 ° , corresponding to amorphous silica [20, 21]. With the increasing dosage of AMM, characteristic peaks turned obvious accordingly. Compared to the standard patterns, the characteristic peaks can be indexed

to relevant molybdenum composites, which demonstrated the existence of molybdenum components. The diffraction peaks of $\text{MoO}_3@\text{SiO}_2\text{-200-X}$ samples were indexed to be $(\text{NH}_4)_2\text{Mo}_4\text{O}_{13}$ (JCPDS: 80-0757) [22] (Figure 2a). With the increasing dosage of AMM, more target material entered into the hollow mesoporous silica spheres and typical XRD patterns of $(\text{NH}_4)_2\text{Mo}_4\text{O}_{13}$ appeared. When the materials were calcined at both 200 °C and 400 °C, NH_3 and H_2O almost released completely, the crystal structure transformed into MoO_3 (JCPDS: 05-0508) [23, 24] (Figure 2b). And characteristic peaks of MoO_3 were observed by the increasing mass ratio of AMM: HMSS, resulting from the bigger MoO_3 nanoparticles.

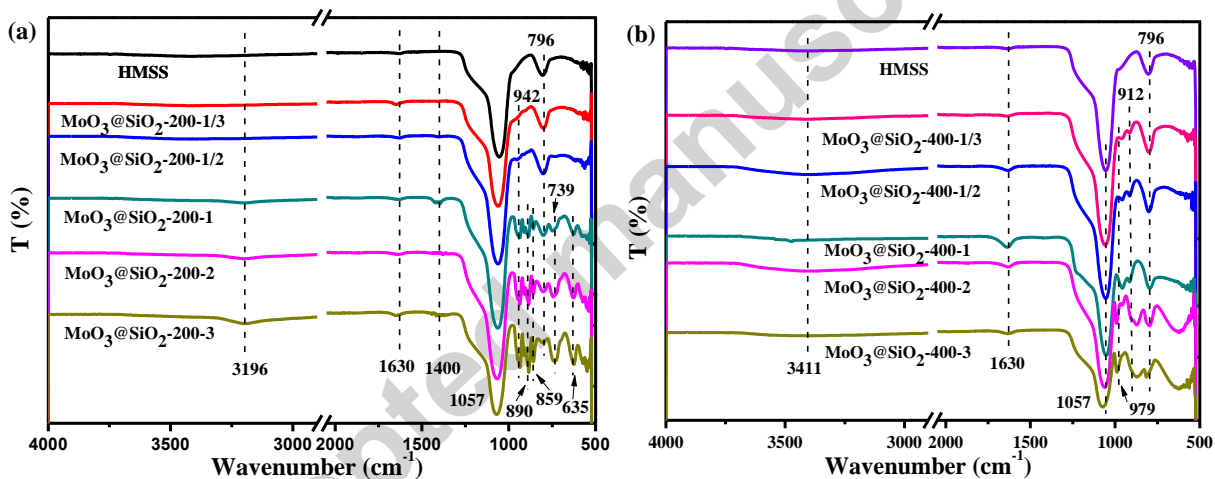
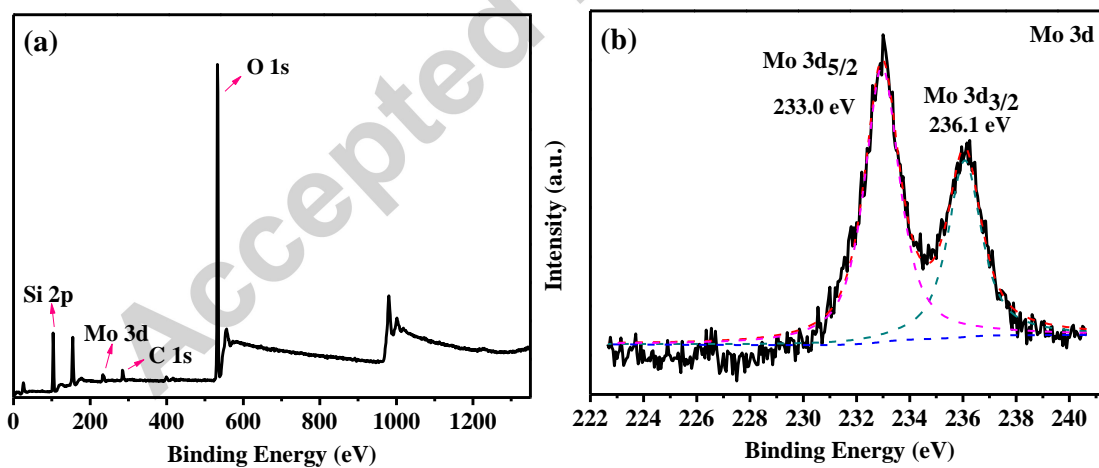


Figure 3. FT-IR spectra of HMSS, $\text{MoO}_3@\text{SiO}_2\text{-200-X}$ (a) and $\text{MoO}_3@\text{SiO}_2\text{-400-X}$ (b).

FT-IR spectra of $\text{MoO}_3@\text{SiO}_2\text{-200-X}$ and $\text{MoO}_3@\text{SiO}_2\text{-400-X}$ were measured in the range of 4000-525 cm^{-1} (Figure 3). NH_3 and H_2O released during the calcination process. When the samples were only treated at 200 °C, weak N-H and O-H deformation bands of ammonium ions and water were observed at 1400 and 1630 cm^{-1} , respectively. The stretching vibrations of O-H and N-H appeared at 3196 cm^{-1} [17]. The vibrational band at 1057 cm^{-1} was assigned as ν_{as} (Si-O-Si) and the band at 796 cm^{-1} was attributed to ν_{s} (Si-O-Si) [25]. With the increasing mass ratio

of AMM and HMSS, characteristic peaks of Mo-O bands appeared below 1000 cm^{-1} . When the samples continued to keep at $400\text{ }^{\circ}\text{C}$ for another 6 h, NH_3 and crystalliferous water almost released completely. The $(\text{NH}_4)_2\text{Mo}_4\text{O}_{13}$ transformed into MoO_3 . Therefore, N-H bands almost disappeared. While adsorbed water and weak stretching vibration of O-H bands at 3411 and 1630 cm^{-1} have been observed, respectively. The vibrational bands of ν_{as} (Si-O-Si) and ν_{s} (Si-O-Si) were still detected at 1057 and 796 cm^{-1} , respectively. Meanwhile, the band at 796 cm^{-1} weakened and some typical peaks of MoO_3 appeared after modification. The peaks at 979 and 912 cm^{-1} were assigned to ν_{s} (Mo=O) and ν_{as} (Mo-O-Mo) for MoO_3 [26-30]. Moreover, with the increasing dosage of AMM, peaks at 979 and 912 cm^{-1} strengthened. For a comparison, the spectrum of $\text{MoO}_3@\text{SiO}_2\text{-200-X}$ and $\text{MoO}_3@\text{SiO}_2\text{-400-X}$ exhibited different Mo-O vibration regions below 1000 cm^{-1} due to different crystal structures. The results of FT-IR indicated the different results after treating with two calcination conditions.



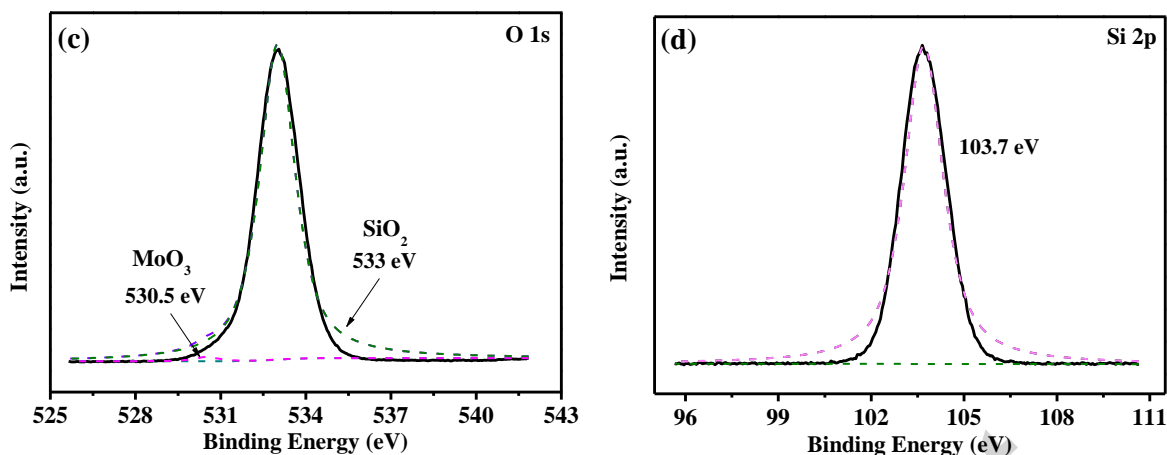
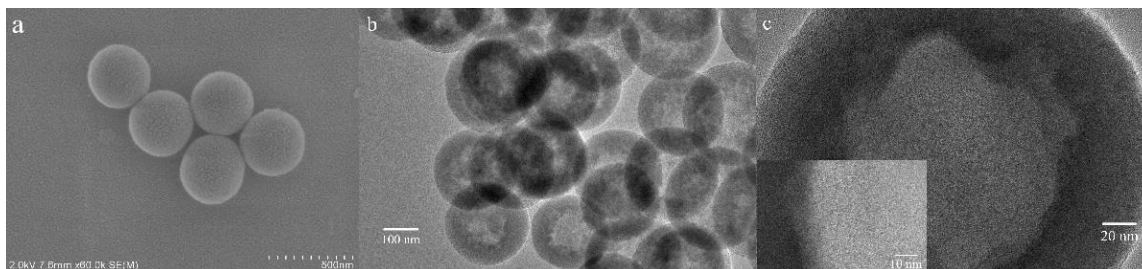


Figure 4. XPS survey spectra (a) and high-resolution spectra of Mo 3d (b), O 1s (c) and Si 2p (d) present in MoO₃@SiO₂-400-1/2.

The elemental composition of material was further characterized by X-ray photoelectron spectroscopy (XPS) using the C 1s peak at 284.8 eV as the reference. The XPS spectra of catalyst MoO₃@SiO₂-400-1/2 were shown in Figure 4. The survey spectrum (Figure 4a) demonstrated that the sample was composed of O, Si and Mo elements. A representative Mo 3d spectra was observed in Figure 4b, the Mo 3d_{3/2} and Mo 3d_{5/2} peaks located at ca. 236.1 and 233.0 eV, respectively. This result implied the formal oxidation state of Mo⁶⁺ in MoO₃ [31, 32]. The O 1s spectra (Figure 4c) could be fitted into two peaks, 530.5 and 533 eV, corresponding to O in trace MoO₃ and abundant SiO₂, respectively [33-36]. In the Si 2p spectra (Figure 4d), the peak at ca. 103.7 eV was attributed to SiO₂ [37].



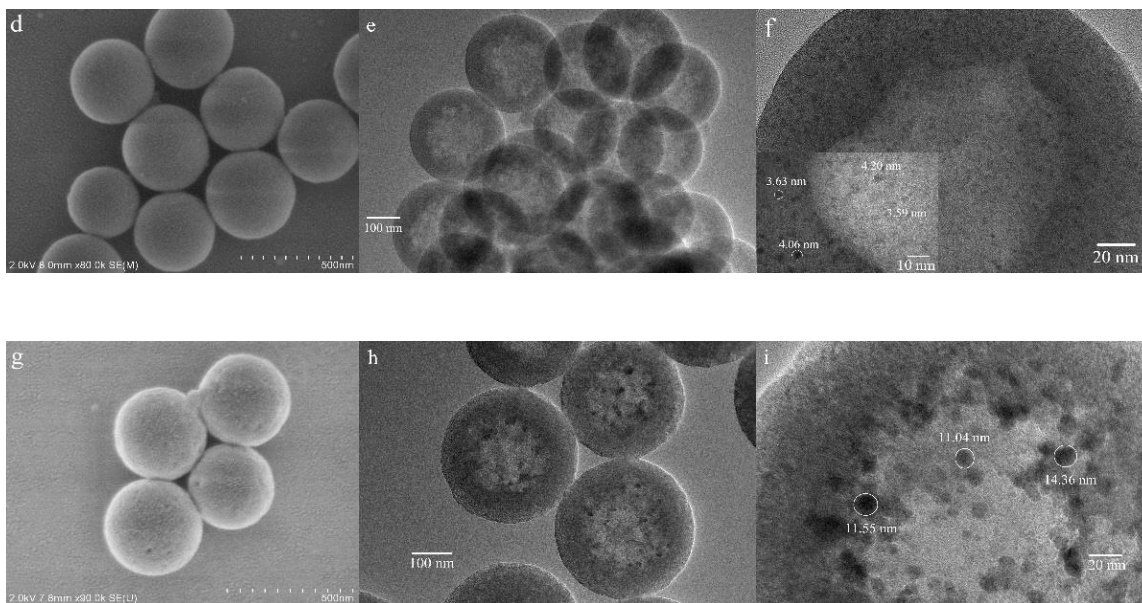


Figure 5. SEM images of HMSS (a), $\text{MoO}_3@\text{SiO}_2\text{-400-1/2}$ (d), and $\text{MoO}_3@\text{SiO}_2\text{-400-1}$ (g), TEM images of HMSS (b, c), $\text{MoO}_3@\text{SiO}_2\text{-400-1/2}$ (e, f) and $\text{MoO}_3@\text{SiO}_2\text{-400-1}$ (h, i).

Morphology of samples were studied by SEM and TEM (Figure 5). Compared with the SEM images, materials maintained the initial structure after modification with MoO_3 . Obviously, TEM images exhibited remarkable changes. Compared with HMSS, $\text{MoO}_3@\text{SiO}_2\text{-400-1/2}$ and $\text{MoO}_3@\text{SiO}_2\text{-400-1}$, dark dots have been observed in $\text{MoO}_3@\text{SiO}_2\text{-400-1/2}$ and $\text{MoO}_3@\text{SiO}_2\text{-400-1}$, especially in $\text{MoO}_3@\text{SiO}_2\text{-400-1}$. These dark dots were supposed to be MoO_3 nanoparticles, which acted as active sites. $\text{MoO}_3@\text{SiO}_2$ nanoreactors with mesoporous shell could prevent aggregation of MoO_3 nanoparticles, which would result in highly dispersed active sites ($\text{MoO}_3@\text{SiO}_2\text{-400-1/2}$ with a size of 4 ± 0.5 nm) and promote the mass diffusion and transport of reactants and products [39]. After treating under high temperature, the active nanoparticles would sinter on the wall of the silica spheres stably. Significantly, since each MoO_3 nanoparticles in the hollow cavity was isolated and had a relatively homogeneous environment, the active sites could fully contact with reactants and improve the reactivity.

Owing to a 67 ± 10 nm shell with wormlike structure, the MoO_3 nanoparticles in cavity would not escape from the nanoreactors. However, with the increasing AMM and HMSS ratio, more molten AMM was introduced into the hollow silica spheres and produced bigger MoO_3 nanoparticles with a size above 10 nm.

Table 1. Textural properties of catalysts.

Sample	BET surface area (m^2/g)	Pore volume (cm^3/g)	Peak in pore size distribution (nm)
HMSS	990	1.06	2.1 and 3.9
$\text{MoO}_3@\text{SiO}_2\text{-400-1/3}$	336	0.50	2.6
$\text{MoO}_3@\text{SiO}_2\text{-400-1/2}$	170	0.19	2.5
$\text{MoO}_3@\text{SiO}_2\text{-400-1}$	97	0.13	2.8
$\text{MoO}_3@\text{SiO}_2\text{-400-2}$	75	0.10	3.0
$\text{MoO}_3@\text{SiO}_2\text{-400-3}$	126	0.20	2.7

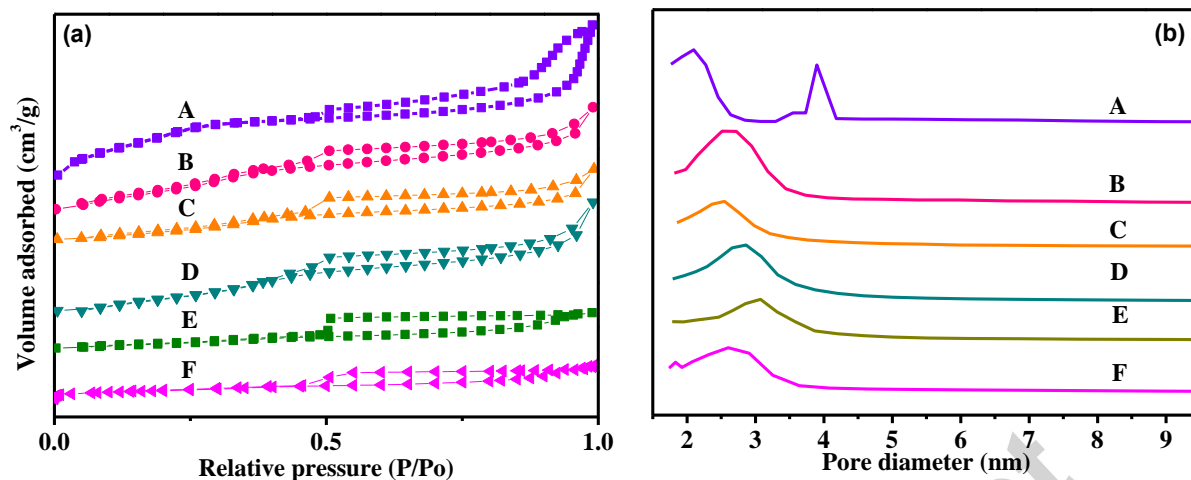


Figure 6. N₂ adsorption-desorption isotherms (a) and the corresponding pore size distributions (b) of HMSS(A), MoO₃@SiO₂-400-1/3 (B), MoO₃@SiO₂-400-1/2 (C), MoO₃@SiO₂-400-1 (D), MoO₃@SiO₂-400-2 (E) and MoO₃@SiO₂-400-3 (F).

Specific surface area and porosity of the materials (HMSS, MoO₃@SiO₂-400-X and MoO₃@SiO₂-200-X) were investigated by N₂ adsorption-desorption measurements (Table 1 and S1, Figure 6 and S1). Figure 6a revealed N₂ adsorption-desorption curves of HMSS, MoO₃@SiO₂-400-1/3, MoO₃@SiO₂-400-1/2, MoO₃@SiO₂-400-1, MoO₃@SiO₂-400-2 and MoO₃@SiO₂-400-3 with a type IV isotherm and H4 hysteresis loop, indicating the formation of mesoporous structure [40]. The corresponding pore size distributions were presented in Figure 6b and Table 1. All the samples exhibited a pore distribution ranged around 2-3 nm. As shown in Table 1, Brunauer-Emmett-Teller (BET) surface area and pore volume of HMSS was 990 m²/g and 1.06 cm³/g, respectively. However, BET surface area and pore volume of MoO₃@SiO₂ nanoreactors dramatically decreased with the increasing AMM: HMSS ratio. The molten AMM diffused into the shell and hollow cavity and transformed to MoO₃ after calcination. These MoO₃ blocked in pores leading to the depression in BET surface area and pore volume. When the

AMM: HMSS ratio increased to 3, abundant MoO_3 nanoparticles appeared and the increasing tendency were supposed to be aggregation of MoO_3 nanoparticles. The peak pore size distribution of HMSS were 2.1 and 3.9 nm. When molybdenum composites introduced, channels were blocked and made the peak pore size distribution move to ca. 2-3 nm. $\text{MoO}_3@SiO_2-200-X$ exhibited the similar results and regulations compared with $\text{MoO}_3@SiO_2-400-X$ (shown in Table S1 and Figure S1).

3.2. Catalytic epoxidation activity

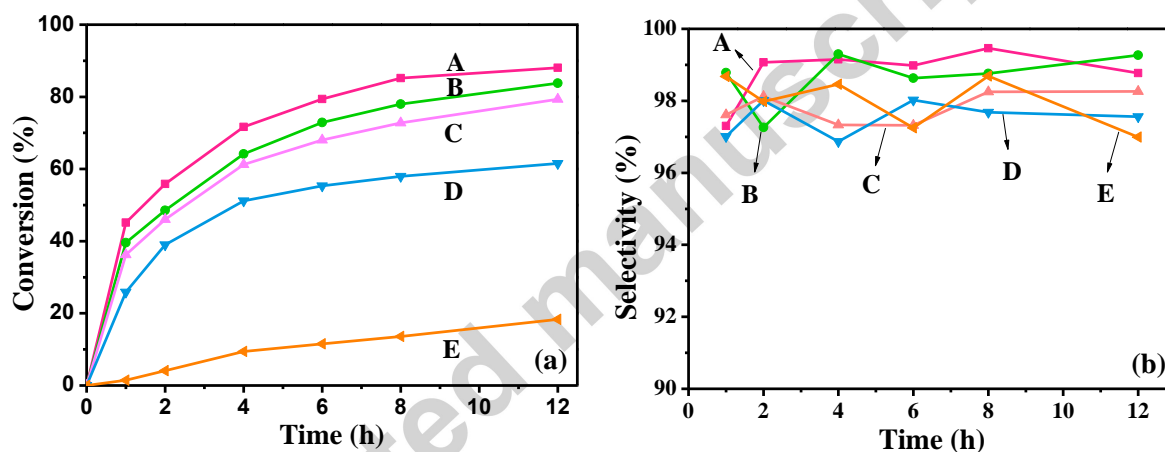


Figure 7. Epoxidation of catalysts with different AMM: HMSS ratio using $\text{MoO}_3@SiO_2-200-X$ as catalysts, (a) conversion, (b) selectivity.

Reaction conditions: catalyst (25 mg), cyclooctene (2.5 mmol), H_2O_2 (50 wt%, 5.0 mmol), acetonitrile (10 mL), n-octane (1.25 mmol), temperature 70 °C. $\text{MoO}_3@SiO_2-200-1/2$ (A), $\text{MoO}_3@SiO_2-200-2$ (B), $\text{MoO}_3@SiO_2-200-1$ (C), $\text{MoO}_3@SiO_2-200-1/3$ (D) and $\text{MoO}_3@SiO_2-200-3$ (E).

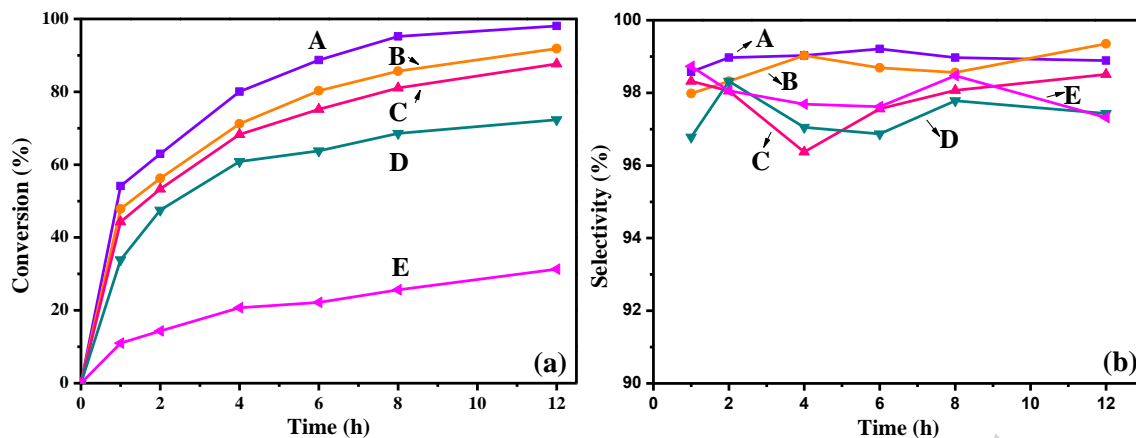


Figure 8. Epoxidation of catalysts with different AMM: HMSS ratio using $\text{MoO}_3@\text{SiO}_2\text{-400-X}$ as catalysts, (a) conversion, (b) selectivity.

Reaction conditions: catalyst (25 mg), cyclooctene (2.5 mmol), H_2O_2 (50 wt%, 5.0 mmol), acetonitrile (10 mL), n-octane (1.25 mmol), temperature 70 °C. $\text{MoO}_3@\text{SiO}_2\text{-400-1/2}$ (A), $\text{MoO}_3@\text{SiO}_2\text{-400-2}$ (B), $\text{MoO}_3@\text{SiO}_2\text{-400-1}$ (C), $\text{MoO}_3@\text{SiO}_2\text{-400-1/3}$ (D) and $\text{MoO}_3@\text{SiO}_2\text{-400-3}$ (E).

Table 2. Results of epoxidation of cyclooctene using $\text{MoO}_3@\text{SiO}_2\text{-400-X}$ as catalysts.

Entry	Catalyst	Mo (wt%)	Yield (%)	TOF (h^{-1})
1	$\text{MoO}_3@\text{SiO}_2\text{-400-1/3}$	1.63	33	137
2	$\text{MoO}_3@\text{SiO}_2\text{-400-1/2}$	3.39	54	151

3	MoO ₃ @SiO ₂ -400-1	6.59	44	64
4	MoO ₃ @SiO ₂ -400-2	11.90	38	38
5	MoO ₃ @SiO ₂ -400-3	16.38	11	7

Reaction conditions: catalyst (25 mg), cyclooctene (2.5 mmol), H₂O₂ (50 wt%, 5.0 mmol), acetonitrile (10 mL), n-octane (1.25 mmol), temperature 70 °C, reaction time (2 h).

The reactivity of MoO₃@SiO₂-200-X and MoO₃@SiO₂-400-X was investigated by epoxidation of cyclooctene under neat conditions. Compared with Figure 7 and 8, MoO₃@SiO₂-400-X exhibited better reactivity than MoO₃@SiO₂-200-X. It was supposed to be the incompletely decomposed molybdenum compounds in hollow mesoporous silica spheres. The result was accordance with the result of XRD and FT-IR. MoO₃@SiO₂-200-X displayed certain reactivity in epoxidation of cyclooctene. After NH₃ and H₂O releasing, (NH₄)₆Mo₇O₂₄·4H₂O in MoO₃@SiO₂-200-X transformed into major (NH₄)₂Mo₄O₁₃. MoO₃ was more efficient performance in epoxidation than (NH₄)₂Mo₄O₁₃, which made MoO₃@SiO₂-400-X display superior reactivity than MoO₃@SiO₂-200-X. And as shown in Figure 8, MoO₃@SiO₂-400-1/2 was found to give the optimal reactivity. With the increasing of AMM: HMSS mass ratio, content of MoO₃ increased. So MoO₃@SiO₂-400-1/2 resulted in higher conversion than MoO₃@SiO₂-400-1/3. However, a large AMM: HMSS ratio would cause blockage in mesoporous shell, which would weaken the transportation of reactants and products, leading to a lower conversion. Meanwhile, higher AMM: HMSS ratio would contribute to bigger active sites, which would also exhibit lower reactivity compared with MoO₃@SiO₂-400-1/2 with highly dispersed active sites. In conclusion, the optimal AMM: HMSS ratio was observed to be 1/2.

According to the results from Table 2, it can be seen that $\text{MoO}_3@\text{SiO}_2\text{-400-1/2}$ had the optimal TOF value of 151 h^{-1} .

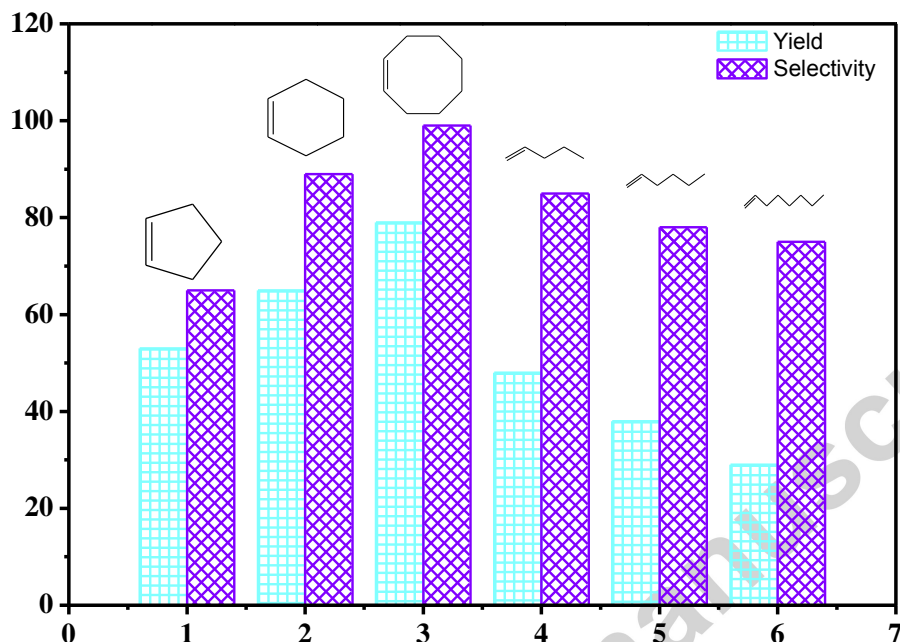


Figure 9. Epoxidation of different alkenes using $\text{MoO}_3@\text{SiO}_2\text{-400-1/2}$ as catalyst.

Reaction conditions: catalyst (25 mg, $\text{MoO}_3@\text{SiO}_2\text{-400-1/2}$), alkene (2.5 mmol), H_2O_2 (50 wt%, 5.0 mmol), acetonitrile (10 mL), n-octane (1.25 mmol), temperature $70 \text{ }^\circ\text{C}$, reaction time (4 h).

In order to research the general applicability of catalysts, catalytic epoxidation of different kinds of olefins was further measured. Epoxidation of cyclic alkenes and terminal linear alkenes was carried out to study the reactivity of different alkenes (Figure 9). Cyclic alkenes exhibited higher reactivity than terminal linear alkenes with the increasing number of carbon atoms which would attribute to more electron donating $(\text{CH}_2)_n$ bridge groups connected to the double bond [41]. The conversion increased in the order of cyclooctene > cyclohexene > cyclopentene. For terminal linear alkenes, the conversion increased in the order of 1-pentene > 1-hexene > 1-

octene. With the increasing number of chain length, cross-linking and attraction between the molecules of the linear olefin, interactions including van der Waals forces, hydrogen bond existed between molecules resulted in forming a so-called “macromolecule” [42]. The probability of linear alkenes in contact with active sites became smaller and the transportation of reactants and products in and outside the shell was found to be difficult, leading to the decrease in reactivity.

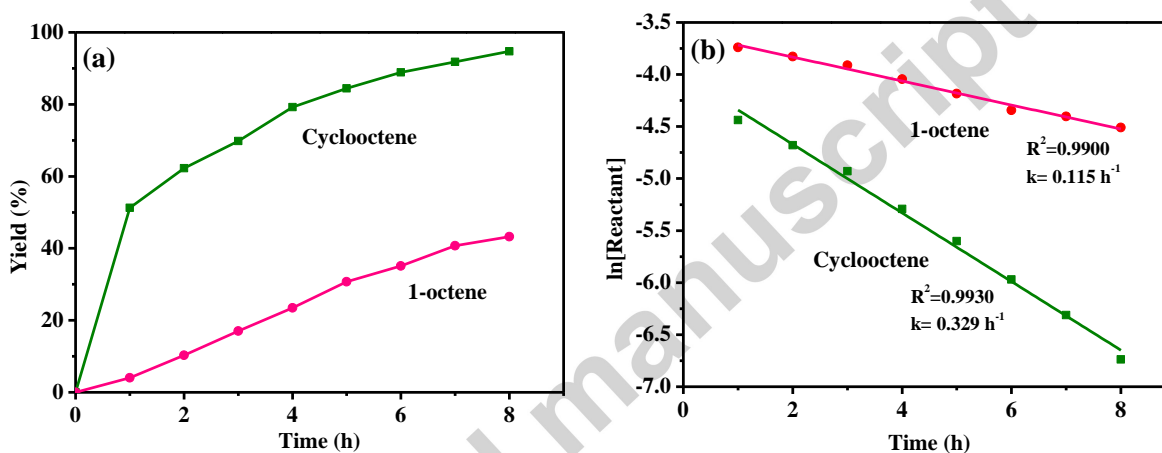


Figure 10. (a) Product yield versus time in epoxidation of various olefins using $\text{MoO}_3@\text{SiO}_2\text{-400-1/2}$ catalyst. (b) The kinetic plots of epoxidation of various olefins using $\text{MoO}_3@\text{SiO}_2\text{-400-1/2}$ catalyst.

Reaction conditions: catalyst (25 mg, $\text{MoO}_3@\text{SiO}_2\text{-400-1/2}$), alkene (2.5 mmol), H_2O_2 (50 wt%, 5.0 mmol), acetonitrile (10 mL), n-octane (1.25 mmol), temperature 70°C , reaction time (4 h).

To further confirm the trend of epoxidation, reactions were run by using the rather unreactive 1-octene and the highly reactive cyclooctene as substrates. All reactions were carried out with excess hydrogen peroxide as oxidant. Figure 10a exhibited the concentration of products against time by using $\text{MoO}_3@\text{SiO}_2\text{-400-1/2}$ catalyst. It was observed that the produced epoxides

followed the descending trend of 1, 2- epoxycyclooctane > 1, 2-epoxyoctane. During the first 4 h, all the olefins reacted rapidly to produce epoxides. After 4 h, the reaction rate slowed down and headed to the equilibrium plateau where the reactions were expected to approach the optimum yield. The order of this kind of reaction was derived for epoxidation results of various olefins (Figure 10b). All the epoxidation reactions established similar straight-line plots with regression value (R^2 close to 1). The reactions were deemed to be the first order kinetic reaction whose reaction ratio solely depended on the reactants [43]. Amongst, cyclooctene displayed higher rate constant, with a k value of 0.329 h^{-1} , followed by 1-octene (0.115 h^{-1}). The kinetic behavior was consistent with reports from literatures [44].

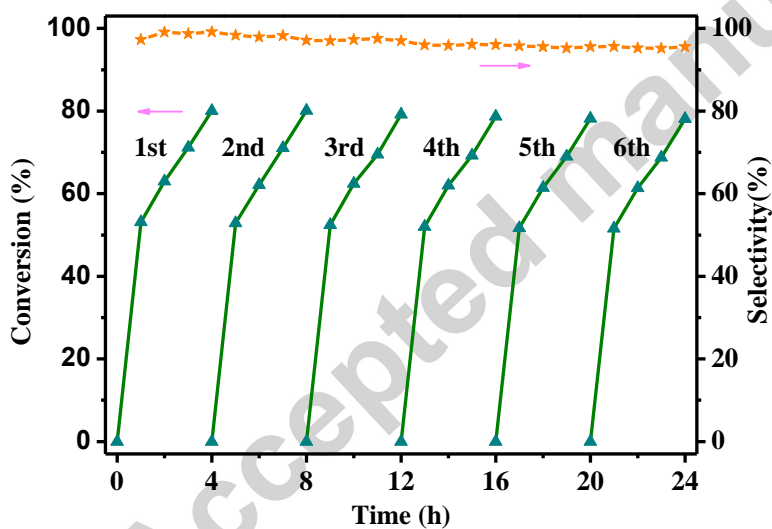


Figure 11. Recycle tests of optimal catalysts via epoxidation of cyclooctene in six consecutive runs.

Reaction conditions: catalyst (25 mg, $\text{MoO}_3@\text{SiO}_2\text{-400-1/2}$), cyclooctene (2.5 mmol), H_2O_2 (50 wt%, 5.0 mmol), acetonitrile (10 mL), n-octane (1.25 mmol), temperature 70°C .

The reusability of catalyst was investigated by using the optimal catalyst ($\text{MoO}_3@\text{SiO}_2\text{-400-1/2}$) in epoxidation of cyclooctene with 50 wt% H_2O_2 as oxidant. The used catalyst was recovered, washed with ethanol, dried and directly utilized in cycling tests without further treatment or regeneration. As shown in Figure 11, $\text{MoO}_3@\text{SiO}_2\text{-400-1/2}$ displayed good stability both of conversion and selectivity. The reactivity was maintained at the same level after six cycles. Channels in shell was wormlike, which was difficult for active sites to escape. Major active sites MoO_3 particles were successfully trapped in the cavity of hollow mesoporous silica spheres. Moreover, minor MoO_3 particles were sintered in channels in shell with wormlike pores under the calcination of 400 °C. Hence, the MoO_3 particles would retain during and after reaction.

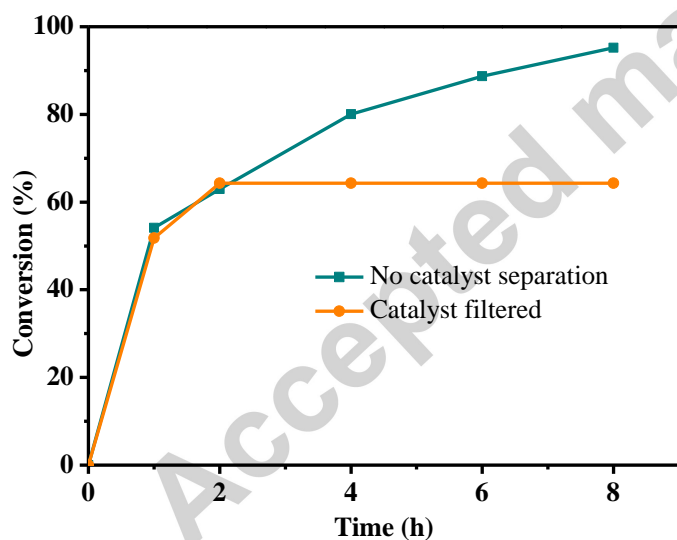


Figure 12. Leaching tests.

Reaction conditions: catalyst (25 mg, $\text{MoO}_3@\text{SiO}_2\text{-400-1/2}$), cyclooctene (2.5 mmol), H_2O_2 (50 wt%, 5.0 mmol), acetonitrile (10 mL), n-octane (1.25 mmol), temperature 70 °C.

To further explain the stability of catalysts, leaching tests were carried out. Hot filtration was exploited during the reaction after reacting for 2 h to separate catalyst [45]. Afterwards, the filtrate continued to react under the same conditions. As shown in Figure 12, no further conversion was observed after separation of catalyst, which demonstrated the stability of catalyst. We believe that the MoO_3 particles have been successfully trapped in hollow mesoporous spheres, which was stable enough to avoid leaching. Furthermore, no molybdenum was observed from the supernatant liquid of epoxidation through ICP-MS whose detection limit of the method is 0.0001 wt%. FT-IR spectra of $\text{MoO}_3@SiO_2-400-1/2$ before and after recycling test were shown in Figure S2. The remained peaks at 979 and 912 cm^{-1} which assigned to ν_s ($\text{Mo}=\text{O}$) and ν_{as} ($\text{Mo}-\text{O}-\text{Mo}$) for MoO_3 indicated the maintained active sites. SEM analysis was used to detect the structure after recycling. As shown in Figure S3, $\text{MoO}_3@SiO_2-400-1/2$ remained the same without breakage after recycling. Both FT-IR and SEM certificated the stability of catalyst.

4. Conclusion

In summary, the facile and efficient fabrication of $\text{MoO}_3@SiO_2$ nanoreactors was successfully developed via a thermal decomposition strategy. The obtained $\text{MoO}_3@SiO_2$ nanoreactors demonstrated a high catalytic activity for epoxidation of alkenes and performed well in the durability and recyclability. Obviously, synthesis of yolk-shell nanoparticles still meets significant conceptual challenges, where most methods involve multi-step approaches and only work successfully on specific cases. This thermal decomposition strategy is easy to operate and can provide a possibility for the fabrication of various kinds of $\text{MoO}_3@shell$ composite nanoreactors and search opportunities for usage in other areas such as drug delivery, lithium-ion batteries and biosensors etc.

Acknowledgements

This work is supported by the Fundamental Research Funds for the Central Universities (JUSRP51507), the Innovation Foundation in Jiangsu Province of China (BY2014023-08) and the Postgraduate Innovation Project of Jiangsu Province (KYLX16_0787).

References

- [1] J. B. Joo, H. Liu, Y. J. Lee, M. Dahl, H. Yu, F. Zaera, Y. Yin, Tailored synthesis of C@TiO₂ yolk-shell nanostructures for highly efficient photocatalysis, *Catal. Today* 264 (2016) 261-269.
- [2] P. Yang, X. Luo, S. Wang, F. Wang, C. Tang, C. Wang, Biodegradable yolk-shell microspheres for ultrasound/MR dual-modality imaging and controlled drug delivery, *Colloid. Surface B* 151 (2017) 333-343.
- [3] R. Zhao, X. Shen, Q. Wu, X. Zhang, W. Li, G. Gao, L. Zhu, L. Ni, G. Diao, M. Chen, Heterogeneous double-shelled constructed Fe₃O₄ yolk-shell magnetite nanoboxes with superior lithium storage performances, *ACS Appl. Mater. Inter.* 9 (2017) 24662-24670.
- [4] M. Q. Wang, C. Ye, S. J. Bao, Y. Zhang, M. W. Xu, Z. Li, Bimetal-organic-frameworks-derived yolk-shell-structured porous Co₂P/ZnO@PC/CNTs hybrids for highly sensitive non-enzymatic detection of superoxide anion released from living cells, *Chem. Commun.* 52 (2016) 12442-12445.
- [5] Y. J. Hong, J. W. Yoon, J. H. Lee, Y. C. Kang, One-pot synthesis of Pd-loaded SnO₂ yolk-shell nanostructures for ultrasensitive methyl benzene sensors, *Chemistry* 20 (2014) 2737-2741.
- [6] S. M. Kim, M. Jeon, K. W. Kim, J. Park, I. S. Lee, Postsynthetic functionalization of a hollow silica nanoreactor with manganese oxide-immobilized metal nanocrystals inside the cavity, *J. Am. Chem. Soc.* 135 (2013) 15714-15717.
- [7] Y. Yang, X. Liu, X. Li, J. Zhao, S. Bai, J. Liu, Q. Yang, A yolk-shell nanoreactor with a basic core and an acidic shell for cascade reactions, *Angew. Chem. Int. Ed.* 124 (2012) 9298-9302.
- [8] T. Zeng, X. Zhang, S. Wang, H. Niu, Y. Cai, Spatial confinement of a Co₃O₄ catalyst in

- hollow metal-organic frameworks as a nanoreactor for improved degradation of organic pollutants, *Environ. Sci. Technol.* 49 (2015) 2350-2357.
- [9] C.-H. Lin, X. Liu, S.-H. Wu, K.-H. Liu, C.-Y. Mou, Corking and uncorking a catalytic yolk-shell nanoreactor: stable gold catalyst in hollow silica nanosphere, *J. Phys. Chem. Lett.* 2 (2011) 2984-2988.
- [10] J. Li, H. C. Zeng, Size tuning, functionalization, and reactivation of Au in TiO₂ nanoreactors, *Angew. Chem. Int. Ed.* 117 (2005) 4416-4419.
- [11] J. Liu, S. Z. Qiao, J. S. Chen, X. W. Lou, X. Xing, G. Q. Lu, Yolk/shell nanoparticles: new platforms for nanoreactors, drug delivery and lithium-ion batteries, *Chem. Commun.* 47 (2011) 12578-12591.
- [12] Z. Zhang, Y. Chen, X. Xu, J. Zhang, G. Xiang, W. He, X. Wang, Well-defined metal-organic framework hollow nanocages, *Angew. Chem. Int. Ed.* 126 (2014) 439-443.
- [13] K. Soni, B. S. Rana, A. K. Sinha, A. Bhaumik, M. Nandi, M. Kumar, G. M. Dhar, 3-D ordered mesoporous KIT-6 support for effective hydrodesulfurization catalysts, *Appl. Catal. B-Environ.* 90 (2009) 55-63.
- [14] S. Ding, J. S. Chen, G. Qi, X. Duan, Z. Wang, E. P. Giannelis, L. A. Archer, X. W. Lou, Formation of SnO₂ hollow nanospheres inside mesoporous silica nanoreactors, *J. Am. Chem. Soc.* 133 (2011) 21-23.
- [15] Y. R. Shen, P. P. Jiang, J. Zhang, G. Bian, P. B. Zhang, Y. M. Dong, W. J. Zhang, Highly dispersed molybdenum incorporated hollow mesoporous silica spheres as an efficient catalyst on epoxidation of olefins, *Mol. Catal.* 433 (2017) 212-223.
- [16] C. Thomazeau, P. A. V. Martin, Effect of support on the thermal decomposition of (NH₄)₆Mo₇O₂₄·4H₂O in the inert gas atmosphere, *Appl. Catal. A-Gen.* 199 (2000) 61-72.
- [17] T. N. Kovács, D. Hunyadi, A. L. A. de Lucena, I. M. Szilágyi, Thermal decomposition of ammonium molybdates, *J. Therm. Anal. Calorim.* 124 (2016) 1013-1021.
- [18] Kh. M. Kadiev, A. M. Gyul'maliev, M. Ya. Shpirt, S. N. Khadzhiev, Thermodynamic and quantum chemical study of the transformations and operation mechanism of molybdenum catalysts under hydrogenation conditions, *Petrol. Chem.* 50 (2010) 312-318.
- [19] D. Zhou, Y. Cui, P. W. Xiao, M. Y. Jiang, B. H. Han, A general and scalable synthesis approach to porous graphene, *Nat. Commun.* 5 (2014) 4716-4723.
- [20] Z. Li, J. Zhao, M. Zhang, J. Xia, A. Meng, SiC nanowires with thickness-controlled SiO₂

- shells: fabrication, mechanism, reaction kinetics and photoluminescence properties, *Nano Res.* 7 (2015) 462-472.
- [21] L. Zheng, F. Gao, S. Zhao, F. Zhou, J. P. Nshimiyimana, X. Diao, Optical design and co-sputtering preparation of high performance Mo-SiO₂ cermet solar selective absorbing coating, *Appl. Surf. Sci.* 280 (2013) 240-246.
- [22] M. Roussel, M. Bouchard, K. Karim, S. Al-Sayari, E. Bordes-Richard, MoVO-based catalysts for the oxidation of ethane to ethylene and acetic acid, *Appl. Catal. A-Gen.* 308 (2006) 62-74.
- [23] L. Wang, G.-H. Zhang, Y.-J. Sun, X.-W. Zhou, K.-C. Chou, Preparation of ultrafine β -MoO₃ from industrial grade MoO₃ powder by the method of sublimation, *J. Phys. Chem. C* 120 (2016) 19821-19829.
- [24] L. Q. Mai, B. Hu, W. Chen, Y. Y. Qi, C. S. Lao, R. S. Yang, Y. Dai, Z. L. Wang, Lithiated MoO₃ nanobelts with greatly improved performance for lithium batteries, *Adv. Mater.* 19 (2007) 3712-3716.
- [25] M. D. Alba, Z. Luan, J. Klinowski, Titanosilicate mesoporous molecular sieve MCM-41: synthesis and characterization, *J. Phys. Chem.* 100 (1996) 2178-2182.
- [26] V. Madhu Mohan, H. Bin, W. Chen, Enhancement of electrochemical properties of MoO₃ nanobelts electrode using PEG as surfactant for lithium battery, *J. Solid State Electr.* 14 (2010) 1769-1775.
- [27] A. Chithambararaj, N. Rajeswari Yogamalar, A. C. Bose, Hydrothermally synthesized δ -MoO₃ and α -MoO₃ nanocrystals: new findings on crystal-structure-dependent charge transport, *Cryst. Growth Des.* 16 (2016) 1984-1995.
- [28] W. G. Klemperer, V. V. Mainz, W. Shum, R. C. Wang, Organosilicates as silica surface models: the molybdenum trioxide complexes R₃SiOMoO₃-, R= phenyl and tert-butyl, *Inorg. Chem.* 24 (1985) 1968-1970.
- [29] X. Zhang, X. Zeng, M. Yang, Y. Qi, Investigation of a Branchlike MoO₃/polypyrrole hybrid with enhanced electrochemical performance used as an electrode in supercapacitors, *ACS Appl. Mater. Interfaces* 6 (2014) 1125-1130.
- [30] T. H. Chiang, H. C. Yeh, A novel synthesis of α -MoO₃ nanobelts and the characterization, *J. Alloy. Compd.* 585 (2014) 535-541.
- [31] S. N. Timmiati, A. A. Jalil, S. Triwahyono, H. D. Setiabudi, N. H. R. Annuar, Formation

- of acidic Brönsted $(\text{MoO}_x)^-(\text{Hy})^+$ evidenced by XRD and 2,6-lutidine FTIR spectroscopy for cumene cracking, *Appl. Catal. A-Gen.* 459 (2013) 8-16.
- [32] C. Ma, J. Zhou, H. Zhu, W. Yang, J. Liu, Y. Wang, Z. Zou, Constructing a high-efficiency $\text{MoO}_3/\text{polyimide}$ hybrid photocatalyst based on strong interfacial interaction, *ACS Appl. Mater. Interfaces* 7 (2015) 14628-14637.
- [33] R. B. Watson, U. S. Ozkan, Spectroscopic and structural characterization of low-level alkali doping effects on Mo/silica-titania catalysts, *J. Phys. Chem. B* 106 (2002) 6930-6941.
- [34] J. Wang, X. Li, S. Zhang, R. Lu, Facile synthesis of ultrasmall monodisperse "raisin-bun"-type $\text{MoO}_3/\text{SiO}_2$ nanocomposites with enhanced catalytic properties, *Nanoscale* 5 (2013) 4823-4828.
- [35] V. A. Yuryev, K. V. Chizh, V. A. Chapnin, S. A. Mironov, V. P. Dubkov, O. V. Uvarov, V. P. Kalinushkin, V. M. Senkov, O. Y. Nalivaiko, A. G. Novikau, P. I. Gaiduk, Pt silicide/poly-Si Schottky diodes as temperature sensors for bolometers, *J. Appl. Phys.* 117 (2015) 204502-204513.
- [36] L. Bian, S. P. Wang, X. B. Ma, The effect of catalyst preparation on the activity of $\text{MoO}_3\text{-SiO}_2$ catalyst in transesterification of diethyl oxalate, *Kinet. Catal.* 55 (2014) 763-769.
- [37] L. Wang, Y. Huang, X. Sun, H. Huang, P. Liu, M. Zong, Y. Wang, Synthesis and microwave absorption enhancement of $\text{graphene@Fe}_3\text{O}_4@\text{SiO}_2@\text{NiO}$ nanosheet hierarchical structures, *Nanoscale* 6 (2014) 3157-3164.
- [38] C. A. H. M. Anwar, R. Bulpett, An XPS study of amorphous MoO_3/SiO films deposited by co-evaporation, *J. Mater. Sci.* 25 (1990) 1784-1788.
- [39] J. Liu, S. Z. Qiao, S. Budi Hartono, G. Q. M. Lu, Monodisperse yolk-shell nanoparticles with a hierarchical porous structure for delivery vehicles and nanoreactors, *Angew. Chem. Int. Ed.* 122 (2010) 5101-5105.
- [40] T. Yang, J. Liu, R. Zhou, Z. Chen, H. Xu, S. Z. Qiao, M. J. Monteiro, N-doped mesoporous carbon spheres as the oxygen reduction reaction catalysts, *J. Mater. Chem. A* 2 (2014) 18139-18146.
- [41] B. Dutta, S. Jana, A. Bhattacharjee, P. Gütllich, S.-I. Iijima, S. Koner, $\gamma\text{-Fe}_2\text{O}_3$ nanoparticle in NaY-zeolite matrix: preparation, characterization, and heterogeneous catalytic epoxidation of olefins, *Inorg. Chim. Acta.* 363 (2010) 696-704.

- [42] J. Zhang, P. Jiang, Y. Shen, W. Zhang, X. Li, Molybdenum(VI) complex with a tridentate Schiff base ligand immobilized on SBA-15 as effective catalysts in epoxidation of alkenes, *Micropor. Mesopor. Mat.* 206 (2015) 161-169.
- [43] A. Berkessel, J. A. Adrio, Kinetic studies of olefin epoxidation with hydrogen peroxide in 1, 1, 1, 3, 3, 3-hexafluoro-2-propanol reveal a crucial catalytic role for solvent clusters, *Adv. Synth. Catal.* 346 (2004) 275-280.
- [44] Y. K. Ooi, L. Yuliati, D. Hartanto, H. Nur, S. L. Lee, Mesostructured TUD-C supported molybdena doped titania as high selective oxidative catalyst for olefins epoxidation at ambient condition, *Micropor. Mesopor. Mat.* 225 (2016) 411-420.
- [45] Y. Qi, Y. Luan, J. Yu, X. Peng, G. Wang, Nanoscaled copper metal-organic framework (MOF) based on carboxylate ligands as an efficient heterogeneous catalyst for aerobic epoxidation of olefins and oxidation of benzylic and allylic alcohols, *Chem. Eur. J.* 21 (2015) 1589-1597.

Highlights

- A thermal decomposition strategy applied in fabricating $\text{MoO}_3@\text{SiO}_2$ nanoreactors
- Efficient catalysts in epoxidation of alkenes with high reactivity and stability
- Kinetics study on epoxidation of alkenes which follows the first order model